

SiT: Exploring Flow and Diffusion-based Generative Models with Scalable Interpolant Transformers

Nanye Ma Mark Goldstein Michael S. Albergo Nicholas M. Boffi
Eric Vanden-Eijnden[†] Saining Xie[†]
New York University

Code: <https://github.com/willisma/SiT>

Abstract

We present Scalable Interpolant Transformers (SiT), a family of generative models built on the backbone of Diffusion Transformers (DiT). The interpolant framework, which allows for connecting two distributions in a more flexible way than standard diffusion models, makes possible a modular study of various design choices impacting generative models built on dynamical transport: using discrete vs. continuous time learning, deciding the objective for the model to learn, choosing the interpolant connecting the distributions, and deploying a deterministic or stochastic sampler. By carefully introducing the above ingredients, SiT surpasses DiT uniformly across model sizes on the conditional ImageNet 256x256 benchmark using the exact same backbone, number of parameters, and GFLOPs. By exploring various diffusion coefficients, which can be tuned separately from learning, SiT achieves an FID-50K score of 2.06.

1. Introduction

Contemporary success in image generation has come from a combination of algorithmic advances and improvements in model architecture and progress in scaling neural network models and data. State-of-the-art diffusion models [25, 51] proceed by incrementally transforming data into Gaussian noise as prescribed by an iterative stochastic process, which can be specified either in discrete or continuous time. At an abstract level, this corruption process can be viewed as defining a time-dependent distribution that is iteratively smoothed from the original data distribution into a standard normal distribution. Diffusion models learn to reverse this corruption process and push Gaussian noise backwards along this connection to obtain data samples. The objects learned to perform this transformation are conventionally either predicting the noise in the corruption process [25] or predicting the score of the distribution connecting the data and the Gaus-

[†]Equal advising.

| Model | Params(M) | Training Steps | FID ↓ |
|------------------|-----------|----------------|-------------|
| DiT-S | 33 | 400K | 68.4 |
| SiT-S | 33 | 400K | 57.6 |
| DiT-B | 130 | 400K | 43.5 |
| SiT-B | 130 | 400K | 33.5 |
| DiT-L | 458 | 400K | 23.3 |
| SiT-L | 458 | 400K | 18.8 |
| DiT-XL | 675 | 400K | 19.5 |
| SiT-XL | 675 | 400K | 17.2 |
| DiT-XL | 675 | 7M | 9.6 |
| SiT-XL | 675 | 7M | 8.6 |
| DiT-XL (cfg=1.5) | 675 | 7M | 2.27 |
| SiT-XL (cfg=1.5) | 675 | 7M | 2.06 |

Table 1. **Scalable Interpolant Transformers.** We systematically vary the following aspects of a generative model: **discrete vs. continuous time**, **model prediction**, **interpolant**, **choice of sampler**. The resulting Scalable Interpolant Transformer (SiT) model, under identical training compute, consistently outperforms the Diffusion Transformer (DiT) in generating 256x256 ImageNet images. All models employ a patch size of 2. In this work, we ask the question: *What is the source of the performance gain?*

sian [62], though alternatives of these choices exist [27, 54].

The neural network architectures used to represent these objects have been shown to perform well on a variety of tasks. While diffusion models were originally built upon a U-Net backbone [25, 52], recent work has highlighted that architectural advances in vision such as the Vision Transformer (ViT) [21] can be incorporated into the standard diffusion model pipeline to improve performance [48]. The aims of [48] were to push improvements on the model side of the duality of algorithm and model.

Orthogonally, significant research effort has gone into exploring the structure of the noising process, which has been shown to lead to performance benefits [32, 35, 36, 58]. Yet, many of these efforts do not move past the notion of passing



Figure 1. Selected samples from SiT-XL models trained on ImageNet [53] at 512×512 and 256×256 resolution with $\text{cfg} = 4.0$, respectively.

data through a diffusion process with an equilibrium distribution, which is a restricted type of connection between the data and the Gaussian. The recently-introduced *stochastic interpolants* [3] lift such constraints and introduce more flexibility in the noise-data connection. In this paper, we further explore its performance in large scale image generation.

Intuitively, we expect that the difficulty of the *learning problem* can be related to both the specific connection chosen and the object that is learned. Our aim is to clarify these design choices, in order to simplify the learning problem and improve performance. To glean where potential benefits arise in the learning problem, we start with Denoising Diffusion Probabilistic Models (DDPMs) and sweep through adaptations of: (i) which object to learn, and (ii) which interpolant to choose to reveal best practices.

In addition to the learning problem, there is a *sampling problem* that must be solved at inference time. It has been acknowledged for diffusion models that sampling can be either deterministic or stochastic [61], and the choice of sampling method can be made after the learning process. Yet, the diffusion coefficients used for stochastic sampling are typically presented as intrinsically tied to the forward noising process, which need not be the case in general.

Throughout this paper, we explore how the design of the interpolant and the use of the resulting model as either a deterministic or a stochastic sampler impact performance. We gradually transition from a typical denoising diffusion model to an interpolant model by taking a series of orthogonal steps in the design space. As we progress, we carefully evaluate how each move away from the diffusion model impacts the performance. In summary, our **main contributions** are:

- By moving from **discrete to continuous time**, changing the **model prediction**, **interpolant**, and the **choice of sampler**, we observe a consistent performance improvement over the Diffusion Transformer (DiT).
- We systematically study where these improvements come from by addressing these factors one by one: learning in continuous time; learning a *velocity* as compared to a *score*; changing the interpolant connecting the the two distributions; and using the velocity in an SDE sampler with particular choices of diffusion coefficients.
- We show that the SDE for the interpolant can be instantiated using just a velocity model, which we use to push the performance of these methods beyond previous results.

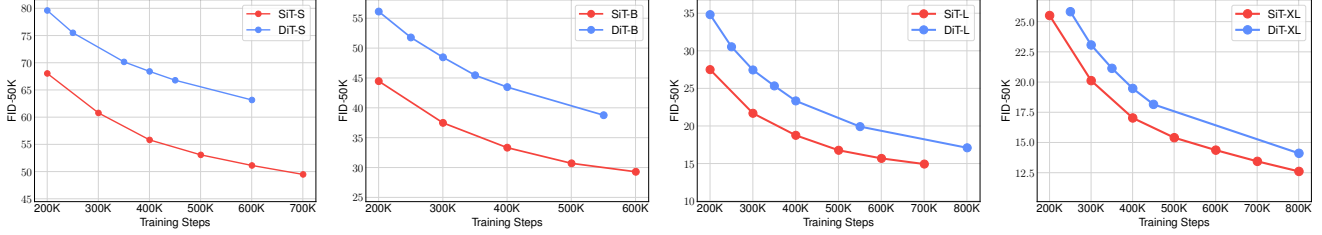


Figure 2. **SiT observes improvement in FID across all model sizes.** We show FID-50K over training iterations for both DiT and SiT. All results are produced by a Euler-Maruyama sampler using 250 integration steps. Across all model sizes, SiT converges much faster.

2. SiT: Scalable Interpolant Transformers

We begin by recalling the main ingredients for building flow-based and diffusion-based generative models.

2.1. Flows and diffusions

In recent years, a flexible class of generative models based on turning noise $\varepsilon \sim \mathcal{N}(0, \mathbf{I})$ into data $\mathbf{x}_* \sim p(\mathbf{x})$ have been introduced. These models use the time-dependent process

$$\mathbf{x}_t = \alpha_t \mathbf{x}_* + \sigma_t \varepsilon, \quad (1)$$

where α_t is a decreasing function of t and σ_t is an increasing function of t . Stochastic interpolants and other flow matching methods [1, 3, 39, 42] restrict the process (1) on $t \in [0, 1]$, and set $\alpha_0 = \sigma_1 = 1$, $\alpha_1 = \sigma_0 = 0$, so that \mathbf{x}_t interpolates exactly between \mathbf{x}_* at time $t = 0$ and ε and time $t = 1$. By contrast, score-based diffusion models [32, 36, 62] set both α_t and σ_t indirectly through different formulations of a stochastic differential equation (SDE) with $\mathcal{N}(0, \mathbf{I})$ as its equilibrium distribution. Moreover, they consider the process \mathbf{x}_t on an interval $[0, T]$ with T large enough that \mathbf{x}_T approximates a Gaussian distribution.

Probability flow. Common to both stochastic interpolants and score-based diffusion models is the observation that the process \mathbf{x}_t can be sampled dynamically using either an SDE or a probability flow ordinary differential equation (ODE). More precisely, the marginal probability distribution $p_t(\mathbf{x})$ of \mathbf{x}_t in (1) coincides with the distribution of the probability flow ODE with a velocity field

$$\dot{\mathbf{X}}_t = \mathbf{v}(\mathbf{X}_t, t), \quad (2)$$

where $\mathbf{v}(\mathbf{x}, t)$ is given by the conditional expectation

$$\begin{aligned} \mathbf{v}(\mathbf{x}, t) &= \mathbb{E}[\dot{\mathbf{x}}_t | \mathbf{x}_t = \mathbf{x}], \\ &= \dot{\alpha}_t \mathbb{E}[\mathbf{x}_* | \mathbf{x}_t = \mathbf{x}] + \dot{\sigma}_t \mathbb{E}[\varepsilon | \mathbf{x}_t = \mathbf{x}]. \end{aligned} \quad (3)$$

Equation (3) is derived in Appendix A.1. By solving the probability flow ODE (2) backwards in time from $\mathbf{X}_T = \varepsilon \sim \mathcal{N}(0, \mathbf{I})$, we can generate samples from $p_0(\mathbf{x})$, which approximates the ground-truth data distribution $p(\mathbf{x})$. We refer to (2) as a *flow-based* generative model.

Reverse-time SDE. The time-dependent probability distribution $p_t(\mathbf{x})$ of \mathbf{x}_t also coincides with the distribution of the reverse-time SDE [5]

$$d\mathbf{X}_t = \mathbf{v}(\mathbf{X}_t, t)dt + \frac{1}{2}w_t s(\mathbf{X}_t, t)dt + \sqrt{w_t}d\bar{\mathbf{W}}_t, \quad (4)$$

where $\bar{\mathbf{W}}_t$ is a reverse-time Wiener process, $w_t > 0$ is an arbitrary time-dependent diffusion coefficient, $\mathbf{v}(\mathbf{x}, t)$ is the velocity defined in (3), and where $s(\mathbf{x}, t) = \nabla \log p_t(\mathbf{x})$ is the score. Similar to \mathbf{v} , this score is given by the conditional expectation

$$s(\mathbf{x}, t) = -\sigma_t^{-1} \mathbb{E}[\varepsilon | \mathbf{x}_t = \mathbf{x}]. \quad (5)$$

This equation is derived in Appendix A.3. Similarly, solving the reverse SDE (4) backwards in time from $\mathbf{X}_T = \varepsilon \sim \mathcal{N}(0, \mathbf{I})$ enables generating samples from the approximated data distribution $p_0(\mathbf{x}) \sim p(\mathbf{x})$. We refer to (2) as a *diffusion-based* generative model.

Design choices. Score-based diffusion models typically tie the choice of α_t , σ_t , and w_t in (4) to the drift and diffusion coefficients used in the forward SDE that generates \mathbf{x}_t (see (10) below). The stochastic interpolant framework decouples the formulation of \mathbf{x}_t from the forward SDE and shows that there is more flexibility in the choices of α_t , σ_t , and w_t . Below, we will exploit this flexibility to construct generative models that outperform score-based diffusion models on standard benchmarks in image generation task.

2.2. Estimating the score and the velocity

Practical use of the probability flow ODE (2) and the reverse-time SDE (4) as generative models relies on our ability to estimate the velocity $\mathbf{v}(\mathbf{x}, t)$ and/or score $s(\mathbf{x}, t)$ fields that enter these equations. The key observation made in score-based diffusion models is that the score can be estimated parametrically as $s_\theta(\mathbf{x}, t)$ using the loss

$$\mathcal{L}_s(\theta) = \int_0^T \mathbb{E}[\|\sigma_t s_\theta(\mathbf{x}_t, t) + \varepsilon\|^2] dt. \quad (6)$$

This loss can be derived by using (5) along with standard properties of the conditional expectation. Similarly, the

velocity in (3) can be estimated parametrically as $\mathbf{v}_\theta(\mathbf{x}, t)$ via the loss

$$\mathcal{L}_v(\theta) = \int_0^T \mathbb{E}[\|\mathbf{v}_\theta(\mathbf{x}_t, t) - \dot{\alpha}_t \mathbf{x}_* - \dot{\sigma}_t \varepsilon\|^2] dt. \quad (7)$$

We note that any time-dependent weight can be included under the integrals in both (6) and (7). These weight factors are key in the context of score-based models when T becomes large [35]; in contrast, with stochastic interpolants where $T = 1$ without any bias, these weights are less important and might impose numerical stability issue (see Appendix B).

Model prediction. We observed that only one of the two quantities $\mathbf{s}_\theta(\mathbf{x}, t)$ and $\mathbf{v}_\theta(\mathbf{x}, t)$ needs to be estimated in practice. This follows directly from the constraint

$$\begin{aligned} \mathbf{x} &= \mathbb{E}[\mathbf{x}_t | \mathbf{x}_t = \mathbf{x}], \\ &= \alpha_t \mathbb{E}[\mathbf{x}_* | \mathbf{x}_t = \mathbf{x}] + \sigma_t \mathbb{E}[\varepsilon | \mathbf{x}_t = \mathbf{x}], \end{aligned} \quad (8)$$

which can be used to re-express the score (5) in terms of the velocity (3) as

$$\mathbf{s}(\mathbf{x}, t) = \sigma_t^{-1} \frac{\alpha_t \mathbf{v}(\mathbf{x}, t) - \dot{\alpha}_t \mathbf{x}}{\dot{\alpha}_t \sigma_t - \alpha_t \dot{\sigma}_t}. \quad (9)$$

We will use this relation to specify our **model prediction**. Conversely, we can also express $\mathbf{v}(\mathbf{x}, t)$ in terms of $\mathbf{s}(\mathbf{x}, t)$. In our experiments, we typically learn the velocity field $\mathbf{v}(\mathbf{x}, t)$ and use it to express the score $\mathbf{s}(\mathbf{x}, t)$ when using an SDE for sampling. We include a detailed derivation in Appendix A.4.

Note that by our definitions $\dot{\alpha}_t < 0$ and $\dot{\sigma}_t > 0$, so that the denominator of (9) is never zero. Yet, σ_t vanishes at $t = 0$, making the σ_t^{-1} in (9) appear to cause a singularity there¹. This suggests the choice $w_t = \sigma_t$ in (4) to cancel this singularity (see Appendix A.3), for which we will explore the performance in the numerical experiments.

2.3. Specifying the interpolating process

Score-based diffusion. In Score-Based Diffusion Models (SBDM), the choice of α_t and σ_t in (1) is typically determined by the choice of the forward SDE used to define this process, though recent work has tried to reconsider this [32, 35]. For example, if we use the standard variance-preserving (VP) SDE [62]

$$d\mathbf{X}_t = -\frac{1}{2}\beta_t \mathbf{X}_t dt + \sqrt{\beta_t} d\mathbf{W}_t \quad (10)$$

for some $\beta_t > 0$, it can be shown (see Appendix B) that the solution to (10) has the same probability distribution $p_t(\mathbf{x})$

¹We remark that $\mathbf{s}(\mathbf{x}, t)$ can be shown to be non-singular at $t = 0$ analytically if the data distribution $p(\mathbf{x})$ has a smooth density [3], though this singularity appears in numerical implementations and losses in general.

as the process \mathbf{x}_t defined in (1) for the choice

$$\text{VP: } \alpha_t = e^{-\frac{1}{2} \int_0^t \beta_s ds}, \quad \sigma_t = \sqrt{1 - e^{-\int_0^t \beta_s ds}}. \quad (11)$$

The only design flexibility in (11) comes from the choice of β_t , because it determines both α_t and σ_t ². For example, setting $\beta_t = 1$ leads to $\alpha_t = e^{-t}$ and $\sigma_t = \sqrt{1 - e^{-2t}}$. This choice necessitates taking T sufficiently large [25] or searching for more appropriate choices of β_t [16, 58, 62] to reduce the bias induced by the fact that the solution to the SDE (10) only converges to $\varepsilon \sim \mathcal{N}(0, \mathbf{I})$ as $t \rightarrow \infty$.

General interpolants. In the stochastic interpolant framework, the process (1) is defined explicitly and without any reference to a forward SDE, creating more flexibility in the choice of α_t and σ_t . Specifically, any choice satisfying:

- (i) $\alpha_t^2 + \sigma_t^2 > 0$ for all $t \in [0, 1]$;
- (ii) α_t and σ_t are differentiable for all $t \in [0, 1]$;
- (iii) $\alpha_1 = \sigma_0 = 0, \alpha_0 = \sigma_1 = 1$;

gives a process that interpolates without bias between $\mathbf{x}_{t=0} = \mathbf{x}_*$ and $\mathbf{x}_{t=1} = \varepsilon$. In our numerical experiments, we exploit this design flexibility to test, in particular, the choices

$$\begin{aligned} \text{Linear:} \quad & \alpha_t = 1 - t, & \sigma_t &= t, \\ \text{GVP:} \quad & \alpha_t = \cos(\frac{1}{2}\pi t), & \sigma_t &= \sin(\frac{1}{2}\pi t), \end{aligned} \quad (12)$$

where GVP refers to a generalized VP which has constant variance across time for any endpoint distributions with the same variance. We note that the fields $\mathbf{v}(\mathbf{x}, t)$ and $\mathbf{s}(\mathbf{x}, t)$ entering (2) and (4) depend on the choice of α_t and σ_t , and typically must be specified before learning³. This is in contrast to the diffusion coefficient $w(t)$, as we now describe.

2.4. Specifying the diffusion coefficient

As stated earlier, the SBDM diffusion coefficient used in the reverse SDE (4) is usually taken to match that of the forward SDE (10). That is, one sets $w_t = \beta_t$. In the stochastic interpolant framework, this choice is again subject to greater flexibility: *any* $w_t > 0$ can be used. Interestingly, this choice can be made *after* learning, as it does not affect the velocity $\mathbf{v}(\mathbf{x}, t)$ or the score $\mathbf{s}(\mathbf{x}, t)$. In our experiments, we exploit this flexibility by considering the choices listed in Table 2.

2.5. Time-discretization and link with DDPM

During inference, continuous time models must be discretized when solving the probability flow ODE (2) and the reverse-time SDE (4). This allows us to make a link with DDPMs [25].

²VP is the only linear scalar SDE with an equilibrium distribution [58]; interpolants extend beyond $\alpha_t^2 + \sigma_t^2 = 1$ by foregoing the requirement of an equilibrium distribution.

³The requirement to learn and sample under one choice of path specified by α_t, σ_t , at training time may be relaxed and is explored in [2].

Increasing transformer sizes \rightarrow

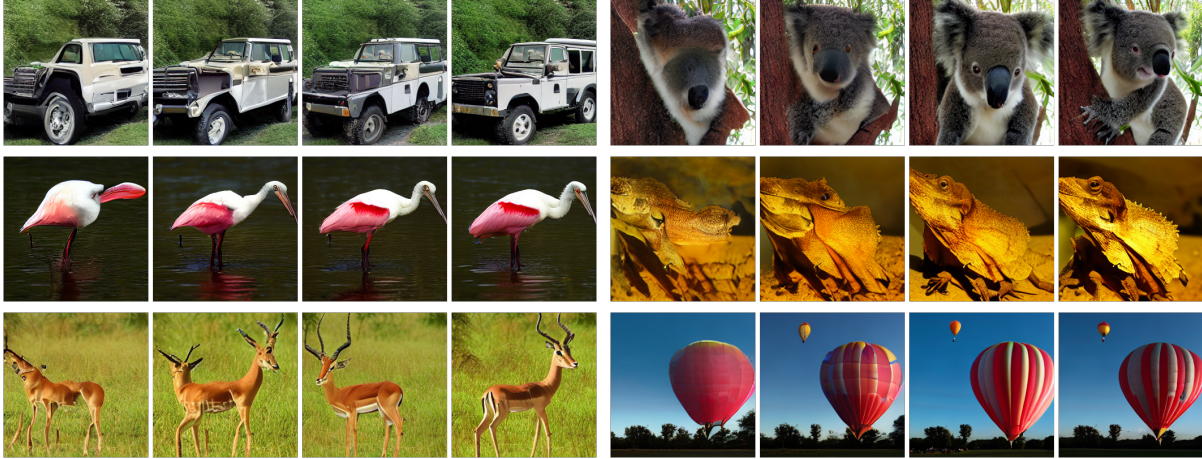


Figure 3. **Increasing transformer size increases sample quality.** *Best viewed zoomed-in.* We sample from all 4 of our SiT model (SiT-S, SiT-B, SiT-L and SiT-XL) after 400K training steps using the same latent noise and class label.

| Expression for w_t |
|---|
| $\beta_t = -2\sigma_t(\dot{\sigma}_t - \frac{\sigma_t \dot{\alpha}_t}{\alpha_t})$ |
| σ_t |
| $1 - t$ |
| $\sin^2(\pi t)$ |
| $(\cos(\pi t) + 1)^2$ |
| $(\cos(\pi t) - 1)^2$ |

Table 2. **Diffusion coefficients.** They can be specified after learning to maximize performance. $w_t = \beta_t$ in the first row corresponds to SBDM (see Eq. (11)), which is coupled to the forward process. A detailed derivation is provided in Appendix B. $w_t = \sigma_t$ in the second row is used to eliminate the singularity at $t = 0$ following the explanation at the end of Sec. 2.2. In other choices we decouple w_t from the interpolant and experiment with removing diffusivity at different times in sampling.

Assuming that we discretize time using a grid $0 = t_0 < t_1 < t_2 < \dots < t_N = T$, the process (1) can be evaluated at each grid point, $\mathbf{x}_{t_i} = \alpha_{t_i} \mathbf{x}_* + \sigma_{t_i} \varepsilon$, and both the velocity and the score can be estimated on these points via the losses

$$\mathcal{L}_s^N(\theta) = \sum_{i=0}^N \mathbb{E}[\|\sigma_{t_i} \mathbf{s}_\theta(\mathbf{x}_{t_i}, t_i) + \varepsilon\|^2], \quad (13)$$

$$\mathcal{L}_v^N(\theta) = \sum_{i=0}^N \mathbb{E}[\|\mathbf{v}_\theta(\mathbf{x}_{t_i}, t_i) - \dot{\alpha}_{t_i} \mathbf{x}_* - \dot{\sigma}_{t_i} \varepsilon\|^2]. \quad (14)$$

Moreover, only the learned $\mathbf{s}_\theta(\mathbf{x}, t_i)$ or $\mathbf{v}_\theta(\mathbf{x}, t_i)$ is needed to integrate the probability flow ODE (2) and the reverse-time SDE (4) on the same grid. The resulting procedure, in which we define \mathbf{x}_t iteratively on the grid, is a generalization

of DDPM. Starting from $\mathbf{x}_{t_0} = \mathbf{x}_*$, we set for $i \geq 0$,

$$\mathbf{x}_{t_{i+1}} = \sqrt{1 - h\beta_{t_i}} \mathbf{x}_{t_i} + \sqrt{h\beta_{t_i}} \varepsilon_{t_i}, \quad (15)$$

where $h = t_{i+1} - t_i$ and where we assume that the grid is uniform. Because $\sqrt{1 - h\beta_{t_i}} = 1 - \frac{1}{2}h\beta_{t_i} + o(h)$, it is easy to see that (15) is a consistent time-discretization of the forward SDE (10). Our results show that it is not necessary to specify the time discretized process \mathbf{x}_{t_i} using (15), but instead we can directly use (1) on the time grid.

2.6. Interpolant Transformer Architecture

The backbone architecture and capacity of generative models are also crucial for producing high-quality samples. In order to eliminate any confounding factors and focus on our exploration, we strictly follow the standard Diffusion Transformer (DiT) [48] and its configurations. This way, we can also test the scalability of our model across various model sizes.

Here we briefly introduce the model design. Generating high-resolution images with diffusion models can be computationally expensive. Latent diffusion models (LDMs) [51] address this by first downsampling images into a smaller latent embedding space using an encoder E , and then training a diffusion model on $z = E(x)$. New images are created by sampling z from the model and decoding it back to images using a decoder $x = D(z)$.

Similarly, SiT is also a latent generative model and we use the same pre-trained VAE encoder and decoder models originally used in Stable Diffusion [51]. SiT processes a spatial input z (shape $32 \times 32 \times 4$ for $256 \times 256 \times 3$ images) by first ‘patchifying’ it into T linearly embedded tokens of dimension d . We always use a patch size of 2 in these models as they achieve the best sample quality. We then

| Model | Layers N | Hidden size d | Heads |
|--------|------------|-----------------|-------|
| SiT-S | 12 | 384 | 6 |
| SiT-B | 12 | 768 | 12 |
| SiT-L | 24 | 1024 | 16 |
| SiT-XL | 28 | 1152 | 16 |

Table 3. **Details of SiT models.** We follow DiT [48] for the Small (S), Base (B), Large (L) and XLarge (XL) model configurations.

apply standard ViT [21] sinusoidal positional embeddings to these tokens. We use a series of N SiT transformer blocks, each with hidden dimension d .

Our model configurations—SiT-{S,B,L,XL}—vary in model size (parameters) and compute (flops), allowing for a model scaling analysis. For class-conditional generation on ImageNet, we use the AdaLN-Zero block [48] to process additional conditional information (times and class labels). SiT architectural details are listed in Table 3.

3. Experiments

To provide a more detailed answer to the question raised in Tab. 1 and make a fair comparison between DiT and SiT, we gradually transition from a DiT model (discretized, score prediction, VP interpolant) to a SiT model (continuous, velocity prediction, Linear interpolant) in the following four subsections, and present the impacts on performance. Throughout our experiments in each subsection, we use a DiT-B model at 400K training steps as our backbone. For solving the ODE (2), we adopt a fixed Heun integrator; for solving the SDE (4), we used an Euler-Maruyama integrator. With both solver choices we limit the number of function evaluations (NFE) to be 250 to match the number of sampling steps used in DiT. All numbers presented in the following sections are FID-50K scores evaluated on the ImageNet256 training set.

3.1. Discrete to Continuous Time

To understand the role of continuous-time versus discrete-time models, we study discrete-time DDPM against continuous-time SBDM-VP with estimation of the score. The results are presented in Table 4, where we find a marginal improvement in FID scores when going from a discrete-time denoiser to a continuous-time score field.

| | Model | Objective | FID |
|--|---------|-----------|-----------------------------|
| | DDPM | Noise | \mathcal{L}_s^N 44.2 |
| | SBDM-VP | Score | \mathcal{L}_s 43.6 |

Table 4. **DDPM vs. SBDM.**

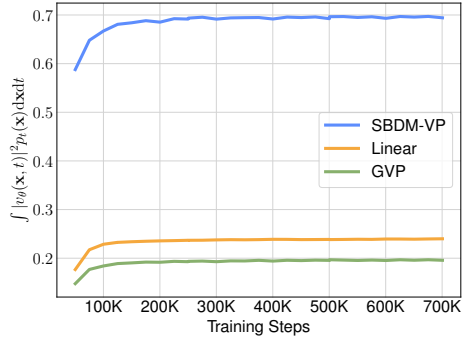


Figure 4. **Path length.** The path length $\mathcal{C}(v) = \int_0^1 \mathbb{E}[|\mathbf{v}(\mathbf{x}_t, t)|^2] dt$ arising from the velocity field at different training steps for the various models considered: SBDM (VP), Linear, and GVP; each curve is approximated by 10000 datapoints.

3.2. Model parameterizations

To clarify the role of the model parameterization in the context of SBDM-VP, we now compare learning (i) a score model using (6), (ii) a weighted score model (see Appendix A.3), or (iii) a velocity model using (7). The results are shown in Table 5, where we find that we obtain a significant performance improvement by learning a weighted score model or a velocity model.

| Interpolant | Model | Objective | ODE |
|-------------|----------|---------------------------|-------------|
| SBDM-VP | Score | \mathcal{L}_s | 43.6 |
| SBDM-VP | Score | \mathcal{L}_{s_λ} | 39.1 |
| SBDM-VP | Velocity | \mathcal{L}_v | 39.8 |

Table 5. **Effect of model parameterization.**

3.3. Choice of interpolant

Section 2 highlights that there are many possible ways to build a connection between the data distribution and a Gaussian by varying the choice of α_t and σ_t in the definition of the interpolant (1). To understand the role of this choice, we now study the benefits of moving away from the commonly-used SBDM-VP setup. We consider learning a velocity model $\mathbf{v}(\mathbf{x}, t)$ with the Linear and GVP interpolants presented in (12), which make the interpolation between the Gaussian and the data distribution exact on $[0, 1]$. We benchmark these models against the SBDM-VP in Table 6, where we find that both the GVP and Linear interpolants obtain significantly improved performance.

One possible explanation for this observation is given in Fig. 4, where we see that the path length (transport cost) is reduced when changing from SBDM-VP to GVP or Linear. Numerically, we also note that for SBDM-VP, $\dot{\sigma}_t = \beta_t e^{-\int_0^t \beta_s ds} / (2\sigma_t)$ becomes singular at $t = 0$: this

can pose numerical difficulties inside \mathcal{L}_v , leading to difficulty in learning near the data distribution. This issue does not appear with the GVP and Linear interpolants.

| <i>Interpolant</i> | <i>Model</i> | <i>Objective</i> | FID |
|--------------------|--------------|------------------|-------------|
| SBDM-VP | Velocity | \mathcal{L}_v | 39.8 |
| Linear | Velocity | \mathcal{L}_v | 34.8 |
| GVP | Velocity | \mathcal{L}_v | 34.6 |

Table 6. Effect of interpolant.

3.4. Deterministic vs stochastic sampling

Using the SBDM diffusion coefficient. As shown in Sec. 2, given a learned model, we can sample using either the probability flow equation (2) or an SDE (4). In SBDM we conventionally take as diffusion coefficient $w_t = \beta_t$. For Linear and GVP interpolant, we follow the derivation in Appendix B to express β_t in terms of α_t and σ_t .

Our results are shown in Tab. 7, where we find performance improvements by sampling with an SDE over the ODE, which is in line with the bounds given in [3]: the SDE has better control over the KL divergence between the time-dependent density at $t = 0$ and the ground truth data distribution. We note that the performance of ODE and SDE integrators may differ under different computation budgets. As shown in Fig. 5, the ODE converges faster with fewer NFE, while the SDE is capable of reaching a much lower final FID score when given a larger computational budget.

| <i>Interpolant</i> | <i>Model</i> | <i>Objective</i> | ODE | SDE |
|--------------------|--------------|------------------|------|-------------|
| SBDM-VP | Velocity | \mathcal{L}_v | 39.8 | 37.8 |
| Linear | Velocity | \mathcal{L}_v | 34.8 | 33.6 |
| GVP | Velocity | \mathcal{L}_v | 34.6 | 32.9 |

Table 7. ODE vs. SDE, SBDM diffusion.

Tunable diffusion coefficient. Motivated by the improved performance of SDE sampling, we now consider the effect of tuning the diffusion coefficient in a manner that is distinct from the choices made in SBDM, as detailed in Tab. 2. As shown in Tab. 8, we find that the optimal choice for sampling is both model prediction and interpolant dependent. We picked the three functions with the best performance and sweep through all different combinations of our model prediction and interpolant, and present the result in Tab. 8.

We also note that the influences of different diffusion coefficients can vary across different model sizes. Empirically, we observe the best choice for our SiT-XL is a velocity model with Linear interpolant and sampled with σ_t coefficient.

3.5. Classifier-free guidance

Classifier-free guidance (CFG) [24] often leads to improved performance for score-based models. In this section, we

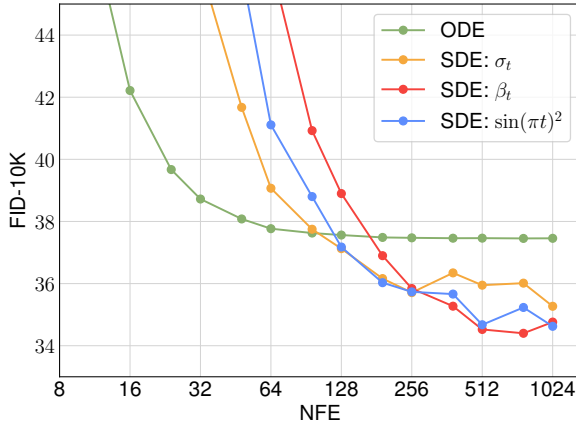


Figure 5. Comparison of ODE and SDE w/ choices of diffusion coefficients. We evaluate each sampler using a 400K steps trained SiT-B model with Linear interpolant and learning the $\mathbf{v}(\mathbf{x}, t)$.

give a concise justification for adopting it on the velocity model, and then empirically show that the drastic gains in performance for DiT case carry across to SiT.

Guidance for a velocity field means that: (i) that the velocity model $\mathbf{v}_\theta(\mathbf{x}, t; \mathbf{y})$ takes class labels y during training, where y is occasionally masked with a null token \emptyset ; and (ii) during sampling the velocity used is $\mathbf{v}_\theta^\zeta(\mathbf{x}, t; \mathbf{y}) = \zeta \mathbf{v}_\theta(\mathbf{x}, t; \mathbf{y}) + (1 - \zeta) \mathbf{v}_\theta(\mathbf{x}, t; \emptyset)$ for a fixed $\zeta > 0$. In Appendix C, we show that this indeed corresponds to sampling the tempered density $p(\mathbf{x}_t)p(\mathbf{y}|\mathbf{x}_t)^\zeta$ as proposed in [46]. Given this observation, one can leverage the usual argument for classifier-free guidance of score-based models.

For a CFG scale of $\zeta = 1.5$, DiT-XL sees an improvement in FID from 9.6 (non-CFG) down to 2.27 (CFG). We observed similar performance improvement with our largest SiT-XL model under identical computation budget and CFG scale. Sampled with an ODE, the FID-50K score improves from 9.4 to 2.15 (Tab. 9 and Appendix D); with an SDE, the FID improves from 8.6 to 2.06 (Tab. 1 and Tab. 9). This shows that SiT benefits from the same training and sampling choices explored previously, and can surpass DiT’s performance in each training setting, not only with respect to model size, but also with respect to sampling choices.

4. Related Work

Transformers. The transformer architecture [66] has emerged as a powerful tool for application domains as diverse as vision [21, 47], language [68, 69], quantum chemistry [67], active matter systems [9], and biology [11]. Several works have built on DiT and have made improvements by modifying the architecture to internally include masked prediction layers [22, 70]; these choices are orthogonal to the transition from DiT to SiT studied in this work; they may be fruitfully combined in future work.

| <i>Interpolant</i> | <i>Model</i> | <i>Objective</i> | $w_t = \beta_t$ | $w_t = \sigma_t$ | $w_t = \sin^2(\pi t)$ |
|--------------------|----------------|---------------------------|-----------------|------------------|-----------------------|
| SBDM-VP | velocity score | \mathcal{L}_v | 37.8 | 38.7 | 39.2 |
| | | \mathcal{L}_{s_λ} | 35.7 | 37.1 | 37.7 |
| GVP | velocity score | \mathcal{L}_v | 32.9 | 33.4 | 33.6 |
| | | \mathcal{L}_s | 38.0 | 33.5 | 33.2 |
| Linear | velocity score | \mathcal{L}_v | 33.6 | 33.5 | 33.3 |
| | | \mathcal{L}_s | 41.0 | 35.3 | 34.4 |

Table 8. **Evaluation of our SDE samplers.** All results in the table are FID-50K scores produced by an SiT-B model at 400K training steps. The last three columns specify different diffusion coefficients w_t detailed in Tab. 2. To make the SBDM-VP competitive when learning a score, we use a weighted score given in Appendix A.4, as per the remarks below (7).

| Class-Conditional ImageNet 256x256 | | | | | |
|-------------------------------------|-------------|-------------|--------|-------------|---------|
| Model | FID↓ | sFID↓ | IS↑ | Precision↑ | Recall↑ |
| BigGAN-deep[10] | 6.95 | 7.36 | 171.4 | 0.87 | 0.28 |
| StyleGAN-XL[55] | 2.30 | 4.02 | 265.12 | 0.78 | 0.53 |
| Mask-GIT[12] | 6.18 | - | 182.1 | - | - |
| ADM[19] | 10.94 | 6.02 | 100.98 | 0.69 | 0.63 |
| ADM-G, ADM-U | 3.94 | 6.14 | 215.84 | 0.83 | 0.53 |
| CDM[26] | 4.88 | - | 158.71 | - | - |
| RIN[30] | 3.42 | - | 182.0 | - | - |
| Simple Diffusion(U-Net)[27] | 3.76 | - | 171.6 | - | - |
| Simple Diffusion(U-ViT, L) | 2.77 | - | 211.8 | - | - |
| VDM++[35] | 2.12 | - | 267.7 | - | - |
| DiT-XL(cfg = 1.5)[48] | 2.27 | 4.60 | 278.24 | 0.83 | 0.57 |
| SiT-XL(cfg = 1.5, ODE) | 2.15 | 4.60 | 258.09 | 0.81 | 0.60 |
| SiT-XL(cfg = 1.5, SDE: σ_t) | 2.06 | 4.50 | 270.27 | 0.82 | 0.59 |

Table 9. **Benchmarking class-conditional image generation on ImageNet 256x256.** SiT-XL surpasses DiT-XL in FID when either of the samplers, ODE or SDE-based.

Training and Sampling in Diffusions. Diffusion models arose from [25, 59, 62] and have close historical relationship with denoising methods [28, 29, 57]. Various efforts have gone into improving the sampling algorithms behind these methods in the context of DDPM [60] and SBDM [32, 61]; these are also orthogonal to our studies and may be combined to push for better performance in future work. Improved Diffusion ODE [71] also studies several combinations of model parameterizations (velocity versus noise) and paths (VP versus Linear) for sampling an ODE; they report best results for velocity model with smoother probability flow; they focus on lower dimensional experiments, benchmark with likelihoods, and do not consider SDE sampling. In our work, we explore the effects of changing between VP, Linear, and GVP interpolants, as well as score and velocity parameterizations in depth and show how these choices individually improve performance on the larger scale ImageNet256. We also document how FIDs change with respect to a family of sampling algorithms including black-box ODEs and SDEs indexed by a choice of diffusion coefficients, and show that

the best coefficient choice may depend on the model and interpolant. This brings the observations about the flexibility and trade-offs of sampling from [3] into practice.

Interpolants and flow matching. Velocity field parameterizations using the Linear interpolant were also studied in [39, 42], and were generalized to the manifold setting in [6]. A trade-off in bounds on the KL divergence between the target distribution and the model arises when considering sampling with SDEs versus ODE; [3] shows that minimizing the objectives presented in this work controls KL for SDEs, but not for ODEs. Error bounds for SDE-based sampling with score-based diffusion models are studied in [13, 14, 37, 38]. Error bounds on the ODE are also explored in [7, 15], in addition to the Wasserstein bounds provided in [1].

Other related works make improvements by changing how noise and data are sampled during training. [50, 64] compute mini-batch optimal couplings between the Gaussian and data distribution to reduce the transport cost and gradient variance; [4] instead build the coupling by flowing directly from the conditioning variable to the data for image-conditional tasks such as super-resolution and in-painting. Finally, various work considers learning a stochastic bridge connecting two arbitrary distributions [18, 41, 49, 56]. These directions are compatible with our investigations; they specify the learning problem for which one can then vary the choices of model parameterizations, interpolant schedules, and sampling algorithms.

Diffusion in Latent Space. Generative modeling in latent space [51, 65] is a tractable approach for modeling high-dimensional data. The approach has been applied beyond images to video generation [8], which is a yet-to-be explored and promising application area for velocity trained models. [17] also train velocity models in the latent space of the pre-trained Stable Diffusion VAE. They demonstrate promising results for the DiT-B backbone with a final FID-50K of 4.46; their study was one motivation for the investigation in this work regarding which aspects of these models contribute to the gains in performance over DiT.

5. Conclusion

In this work, we have presented Scalable Interpolant Transformers, a simple and powerful framework for image generation tasks. Within the framework, we explored the tradeoffs between a number of key design choices: the choice of a continuous or discrete-time model, the choice of interpolant, the choice of model prediction, and the choice of diffusion coefficient. We highlighted the advantages and disadvantages of each choice and demonstrated how careful decisions can lead to significant performance improvements. Many concurrent works [23, 31, 40, 45] explore similar approaches in a wide variety of downstream tasks, and we leave the application of SiT to these tasks for future works.

Acknowledgements. We would like to thank Adithya Iyer, Sai Charitha Akula, Fred Lu, Jitao Gu, and Edwin P. Gerber for helpful discussions and feedback. The research is partly supported by the Google TRC program.

References

- [1] Michael S Albergo and Eric Vanden-Eijnden. Building normalizing flows with stochastic interpolants. In *ICLR*, 2023. 3, 8
- [2] Michael S Albergo, Nicholas M Boffi, Michael Lindsey, and Eric Vanden-Eijnden. Multimarginal generative modeling with stochastic interpolants. *arXiv preprint arXiv:2310.03695*, 2023. 4
- [3] Michael S. Albergo, Nicholas M. Boffi, and Eric Vanden-Eijnden. Stochastic interpolants: A unifying framework for flows and diffusions. *arXiv preprint arXiv:2303.08797*, 2023. 2, 3, 4, 7, 8, 1, 5, 6
- [4] Michael S Albergo, Mark Goldstein, Nicholas M Boffi, Rajesh Ranganath, and Eric Vanden-Eijnden. Stochastic interpolants with data-dependent couplings. *arXiv preprint arXiv:2310.03725*, 2023. 8
- [5] Brian D.O. Anderson. Reverse-time diffusion equation models. *Stochastic Processes and their Applications*, 1982. 3
- [6] Heli Ben-Hamu, Samuel Cohen, Joey Bose, Brandon Amos, Aditya Grover, Maximilian Nickel, Ricky TQ Chen, and Yaron Lipman. Matching normalizing flows and probability paths on manifolds. In *ICML*, 2022. 8
- [7] Joe Benton, George Deligiannidis, and Arnaud Doucet. Error bounds for flow matching methods. *arXiv preprint arXiv:2305.16860*, 2023. 8
- [8] Andreas Blattmann, Robin Rombach, Huan Ling, Tim Dockhorn, Seung Wook Kim, Sanja Fidler, and Karsten Kreis. Align your latents: High-resolution video synthesis with latent diffusion models. In *CVPR*, 2023. 8
- [9] Nicholas M Boffi and Eric Vanden-Eijnden. Deep learning probability flows and entropy production rates in active matter. *arXiv preprint arXiv:2309.12991*, 2023. 7
- [10] Andrew Brock, Jeff Donahue, and Karen Simonyan. Large scale gan training for high fidelity natural image synthesis. In *ICLR*, 2019. 8
- [11] Abel Chandra, Laura Tünnemann, Tommy Löfstedt, and Regina Gratz. Transformer-based deep learning for predicting protein properties in the life sciences. *Elife*, 12:e82819, 2023. 7
- [12] Huiwen Chang, Han Zhang, Lu Jiang, Ce Liu, and William T. Freeman. Maskgit: Masked generative image transformer. In *CVPR*, 2022. 8
- [13] Hongrui Chen, Holden Lee, and Jianfeng Lu. Improved analysis of score-based generative modeling: User-friendly bounds under minimal smoothness assumptions. In *ICML*, 2023. 8
- [14] Sitan Chen, Sinho Chewi, Jerry Li, Yuanzhi Li, Adil Salim, and Anru Zhang. Sampling is as easy as learning the score: theory for diffusion models with minimal data assumptions. In *ICLR*, 2023. 8
- [15] Sitan Chen, Giannis Daras, and Alex Dimakis. Restoration-degradation beyond linear diffusions: A non-asymptotic analysis for DDIM-type samplers. In *ICML*, 2023. 8
- [16] Ting Chen. On the importance of noise scheduling for diffusion models. *arXiv preprint arXiv:2301.10972*, 2023. 4
- [17] Quan Dao, Hao Phung, Binh Nguyen, and Anh Tran. Flow matching in latent space. *arXiv preprint arXiv:2307.08698*, 2023. 8
- [18] Valentin De Bortoli, James Thornton, Jeremy Heng, and Arnaud Doucet. Diffusion schrödinger bridge with applications to score-based generative modeling. In *NeurIPS*, 2021. 8
- [19] Prafulla Dhariwal and Alex Nichol. Diffusion models beat gans on image synthesis. In *NeurIPS*, 2021. 8, 4, 7
- [20] Tim Dockhorn, Arash Vahdat, and Karsten Kreis. Score-based generative modeling with critically-damped langevin diffusion. In *ICLR*, 2022. 6
- [21] Alexey Dosovitskiy, Lucas Beyer, Alexander Kolesnikov, Dirk Weissenborn, Xiaohua Zhai, Thomas Unterthiner, Mostafa Dehghani, Matthias Minderer, Georg Heigold, Sylvain Gelly, Jakob Uszkoreit, and Neil Houlsby. An image is worth 16x16 words: Transformers for image recognition at scale. In *ICLR*, 2021. 1, 6, 7
- [22] Shanghua Gao, Pan Zhou, Ming-Ming Cheng, and Shuicheng Yan. Masked diffusion transformer is a strong image synthesizer. *arXiv preprint arXiv:2303.14389*, 2023. 7
- [23] Agrim Gupta, Lijun Yu, Kihyuk Sohn, Xiuye Gu, Meera Hahn, Li Fei-Fei, Irfan Essa, Lu Jiang, and José Lezama. Photorealistic video generation with diffusion models. *arXiv preprint arXiv:2312.06662*, 2023. 9
- [24] Jonathan Ho and Tim Salimans. Classifier-free diffusion guidance. *arXiv preprint arXiv:2207.12598*, 2022. 7, 4
- [25] Jonathan Ho, Ajay Jain, and Pieter Abbeel. Denoising diffusion probabilistic models. In *NeurIPS*, 2020. 1, 4, 8
- [26] Jonathan Ho, Chitwan Saharia, William Chan, David J. Fleet, Mohammad Norouzi, and Tim Salimans. Cascaded diffusion models for high fidelity image generation. *arXiv preprint arXiv:2106.15282*, 2021. 8
- [27] Emiel Hoogeboom, Jonathan Heek, and Tim Salimans. simple diffusion: End-to-end diffusion for high resolution images. In *ICML*, 2023. 1, 8
- [28] Aapo Hyvärinen. Estimation of non-normalized statistical models by score matching. *JMLR*, 2005. 8

- [29] Aapo Hyvärinen. Sparse code shrinkage: Denoising of non-gaussian data by maximum likelihood estimation. *Neural Computation*, 1999. 8
- [30] Allan Jabri, David Fleet, and Ting Chen. Scalable adaptive computation for iterative generation. In *ICML*, 2023. 8
- [31] Tomas Jakab, Ruining Li, Shangzhe Wu, Christian Rupprecht, and Andrea Vedaldi. Farm3D: Learning articulated 3d animals by distilling 2d diffusion. In *3DV*, 2024. 9
- [32] Tero Karras, Miika Aittala, Timo Aila, and Samuli Laine. Elucidating the design space of diffusion-based generative models. In *NeurIPS*, 2022. 1, 3, 4, 8, 6
- [33] Patrick Kidger. *On Neural Differential Equations*. PhD thesis, University of Oxford, 2021. 6
- [34] Diederik P Kingma and Jimmy Ba. Adam: A method for stochastic optimization. In *ICLR*, 2015. 7
- [35] Diederik P Kingma and Ruiqi Gao. Understanding the diffusion objective as a weighted integral of elbos. *arXiv preprint arXiv:2303.00848*, 2023. 1, 4, 8, 3
- [36] Diederik P. Kingma, Tim Salimans, Ben Poole, and Jonathan Ho. Variational diffusion models. In *NeurIPS*, 2021. 1, 3, 6
- [37] Holden Lee, Jianfeng Lu, and Yixin Tan. Convergence for score-based generative modeling with polynomial complexity. In *NeurIPS*, 2022. 8
- [38] Holden Lee, Jianfeng Lu, and Yixin Tan. Convergence of score-based generative modeling for general data distributions. In *ALT*, 2023. 8
- [39] Yaron Lipman, Ricky T. Q. Chen, Heli Ben-Hamu, Maximilian Nickel, and Matt Le. Flow matching for generative modeling. In *ICLR*, 2023. 3, 8
- [40] Ruoshi Liu, Rundi Wu, Basile Van Hoorick, Pavel Tokmakov, Sergey Zakharov, and Carl Vondrick. Zero-1-to-3: Zero-shot one image to 3d object. In *ICCV*, 2023. 9
- [41] Xingchao Liu, Lemeng Wu, Mao Ye, and Qiang Liu. Let us build bridges: Understanding and extending diffusion generative models. *arXiv preprint arXiv:2208.14699*, 2022. 8
- [42] Xingchao Liu, Chengyue Gong, and Qiang Liu. Flow straight and fast: Learning to generate and transfer data with rectified flow. In *ICLR*, 2023. 3, 8
- [43] Ilya Loshchilov and Frank Hutter. Decoupled weight decay regularization. In *ICLR*, 2019. 7
- [44] Cheng Lu, Yuhao Zhou, Fan Bao, Jianfei Chen, Chongxuan Li, and Jun Zhu. Dpm-solver: A fast ode solver for diffusion probabilistic model sampling in around 10 steps. In *NeurIPS*, 2022. 6
- [45] Chenlin Meng, Yutong He, Yang Song, Jiaming Song, Jiajun Wu, Jun-Yan Zhu, and Stefano Ermon. Sdedit: Guided image synthesis and editing with stochastic differential equations. In *ICLR*, 2022. 9
- [46] Alex Nichol and Prafulla Dhariwal. Improved denoising diffusion probabilistic models. In *ICML*, 2021. 7
- [47] Niki Parmar, Ashish Vaswani, Jakob Uszkoreit, Łukasz Kaiser, Noam Shazeer, Alexander Ku, and Dustin Tran. Image Transformer. In *ICML*, 2018. 7
- [48] William Peebles and Saining Xie. Scalable diffusion models with transformers. In *ICCV*, 2023. 1, 5, 6, 8, 7
- [49] Stefano Peluchetti. Non-denoising forward-time diffusions. In *ICLR*, 2022. 8
- [50] Aram-Alexandre Pooladian, Heli Ben-Hamu, Carles Domingo-Enrich, Brandon Amos, Yaron Lipman, and Ricky T. Q. Chen. Multisample flow matching: Straightening flows with minibatch couplings. In *ICML*, 2023. 8
- [51] Robin Rombach, Andreas Blattmann, Dominik Lorenz, Patrick Esser, and Björn Ommer. High-resolution image synthesis with latent diffusion models. In *CVPR*, 2022. 1, 5, 8
- [52] Olaf Ronneberger, Philipp Fischer, and Thomas Brox. U-net: Convolutional networks for biomedical image segmentation. In *MICCAI*, 2015. 1
- [53] Olga Russakovsky, Jia Deng, Hao Su, Jonathan Krause, Sanjeev Satheesh, Sean Ma, Zhiheng Huang, Andrej Karpathy, Aditya Khosla, Michael Bernstein, et al. Imagenet large scale visual recognition challenge. *IJCV*, 2015. 2
- [54] Tim Salimans and Jonathan Ho. Progressive distillation for fast sampling of diffusion models. In *ICLR*, 2022. 1, 6
- [55] Axel Sauer, Katja Schwarz, and Andreas Geiger. Stylegan-xl: Scaling stylegan to large diverse datasets. In *SIGGRAPH*, 2022. 8
- [56] Yuyang Shi, Valentin De Bortoli, Andrew Campbell, and Arnaud Doucet. Diffusion schrödinger bridge matching. In *NeurIPS*, 2023. 8
- [57] Eero P. Simoncelli and Edward H. Adelson. Noise removal via bayesian wavelet coring. In *ICIP*, 1996. 8
- [58] Raghav Singhal, Mark Goldstein, and Rajesh Ranganath. Where to diffuse, how to diffuse, and how to get back: Automated learning for multivariate diffusions. In *ICLR*, 2023. 1, 4
- [59] Jascha Sohl-Dickstein, Eric Weiss, Niru Maheswaranathan, and Surya Ganguli. Deep unsupervised learning using nonequilibrium thermodynamics. In *ICML*, 2015. 8
- [60] Jiaming Song, Chenlin Meng, and Stefano Ermon. Denoising diffusion implicit models. In *ICLR*, 2021. 8
- [61] Yang Song, Conor Durkan, Iain Murray, and Stefano Ermon. Maximum likelihood training of score-based diffusion models. In *NeurIPS*, 2021. 2, 8, 3
- [62] Yang Song, Jascha Sohl-Dickstein, Diederik P. Kingma, Abhishek Kumar, Stefano Ermon, and Ben Poole. Score-based generative modeling through stochastic differential equations. In *ICLR*, 2021. 1, 3, 4, 8, 6
- [63] Yang Song, Prafulla Dhariwal, Mark Chen, and Ilya Sutskever. Consistency models. In *ICML*, 2023. 6
- [64] Alexander Tong, Nikolay Malkin, Guillaume Hugué, Yanlei Zhang, Jarrid Rector-Brooks, Kilian Fatras, Guy Wolf, and Yoshua Bengio. Improving and generalizing flow-based generative models with minibatch optimal transport. In *ICML Workshop on New Frontiers in Learning, Control, and Dynamical Systems*, 2023. 8
- [65] Arash Vahdat, Karsten Kreis, and Jan Kautz. Score-based generative modeling in latent space. In *NeurIPS*, 2021. 8, 3
- [66] Ashish Vaswani, Noam Shazeer, Niki Parmar, Jakob Uszkoreit, Llion Jones, Aidan N Gomez, Łukasz Kaiser, and Illia Polosukhin. Attention is all you need. In *NeurIPS*, 2017. 7
- [67] Ingrid von Glehn, James S. Spencer, and David Pfau. A Self-Attention Ansatz for Ab-initio Quantum Chemistry. In *ICLR*, 2023. 7

- [68] Qiang Wang, Bei Li, Tong Xiao, Jingbo Zhu, Changliang Li, Derek F Wong, and Lidia S Chao. Learning deep transformer models for machine translation. In *ACL*, 2019. 7
- [69] Manzil Zaheer, Guru Guruganesh, Avinava Dubey, Joshua Ainslie, Chris Alberti, Santiago Ontanon, Philip Pham, Anirudh Ravula, Qifan Wang, Li Yang, and Amr Ahmed. Big Bird: Transformers for Longer Sequences. In *NeurIPS*, 2020. 7
- [70] Hongkai Zheng, Weili Nie, Arash Vahdat, and Anima Anandkumar. Fast training of diffusion models with masked transformers. *arXiv preprint arXiv:2306.09305*, 2023. 7
- [71] Kaiwen Zheng, Cheng Lu, Jianfei Chen, and Jun Zhu. Improved techniques for maximum likelihood estimation for diffusion odes. In *ICML*, 2023. 8

Appendix

A. Proofs

In all proofs below, we use \cdot for dot product and assume all bold notations (\mathbf{x} , $\boldsymbol{\varepsilon}$, etc.) are real-valued vectors in \mathbb{R}^d . Most proofs are derived from Albergo et al. [3].

A.1. Proof of the probability flow ODE (2) with the velocity in Eq. (3).

Consider the time-dependent probability density function (PDF) $p_t(\mathbf{x})$ of $\mathbf{x}_t = \alpha_t \mathbf{x}_* + \sigma_t \boldsymbol{\varepsilon}$ defined in Eq. (1). By definition, its characteristic function $\hat{p}_t(\mathbf{k}) = \int_{\mathbb{R}^d} e^{i\mathbf{k}\cdot\mathbf{x}} p_t(\mathbf{x}) d\mathbf{x}$ is given by

$$\hat{p}_t(\mathbf{k}) = \mathbb{E}[e^{i\mathbf{k}\cdot\mathbf{x}_t}] \quad (16)$$

where \mathbb{E} denotes expectation over \mathbf{x}_* and $\boldsymbol{\varepsilon}$. Taking time derivative on both sides, and using the tower property of conditional expectation, we have

$$\partial_t \hat{p}_t(\mathbf{k}) = i\mathbf{k} \cdot \mathbb{E}[\dot{\mathbf{x}}_t e^{i\mathbf{k}\cdot\mathbf{x}_t}] \quad (17)$$

$$= i\mathbf{k} \cdot \mathbb{E}_{\mathbf{x} \sim p_t}[\mathbb{E}[\dot{\mathbf{x}}_t e^{i\mathbf{k}\cdot\mathbf{x}_t} | \mathbf{x}_t = \mathbf{x}]] \quad (18)$$

$$= i\mathbf{k} \cdot \mathbb{E}_{\mathbf{x} \sim p_t}[\mathbb{E}[(\dot{\alpha}_t \mathbf{x}_* + \dot{\sigma}_t \boldsymbol{\varepsilon}) e^{i\mathbf{k}\cdot\mathbf{x}_t} | \mathbf{x}_t = \mathbf{x}]] \quad (19)$$

$$= i\mathbf{k} \cdot \mathbb{E}_{\mathbf{x} \sim p_t}[\mathbb{E}[(\dot{\alpha}_t \mathbf{x}_* + \dot{\sigma}_t \boldsymbol{\varepsilon}) | \mathbf{x}_t = \mathbf{x}] e^{i\mathbf{k}\cdot\mathbf{x}}] \quad (20)$$

$$= i\mathbf{k} \cdot \mathbb{E}_{\mathbf{x} \sim p_t}[\mathbf{v}(\mathbf{x}, t) e^{i\mathbf{k}\cdot\mathbf{x}}] \quad (21)$$

where $\mathbf{v}(\mathbf{x}, t) = \mathbb{E}[(\dot{\alpha}_t \mathbf{x}_* + \dot{\sigma}_t \boldsymbol{\varepsilon}) | \mathbf{x}_t = \mathbf{x}] = \dot{\alpha}_t \mathbb{E}[\mathbf{x}_* | \mathbf{x}_t = \mathbf{x}] + \dot{\sigma}_t \mathbb{E}[\boldsymbol{\varepsilon} | \mathbf{x}_t = \mathbf{x}]$ is the velocity defined in Eq. (3). Explicitly, Eq. (21) reads

$$\partial_t \int_{\mathbb{R}^d} e^{i\mathbf{k}\cdot\mathbf{x}} p_t(\mathbf{x}) d\mathbf{x} = i\mathbf{k} \cdot \int_{\mathbb{R}^d} \mathbf{v}(\mathbf{x}, t) e^{i\mathbf{k}\cdot\mathbf{x}} p_t(\mathbf{x}) d\mathbf{x} \quad (22)$$

from which we deduce

$$\int_{\mathbb{R}^d} e^{i\mathbf{k}\cdot\mathbf{x}} \partial_t p_t(\mathbf{x}) d\mathbf{x} = \int_{\mathbb{R}^d} \mathbf{v}(\mathbf{x}, t) \cdot \nabla_{\mathbf{x}} [e^{i\mathbf{k}\cdot\mathbf{x}}] p_t(\mathbf{x}) d\mathbf{x} = - \int_{\mathbb{R}^d} \nabla_{\mathbf{x}} \cdot [\mathbf{v}(\mathbf{x}, t) p_t(\mathbf{x})] e^{i\mathbf{k}\cdot\mathbf{x}} d\mathbf{x} \quad (23)$$

where $\nabla_{\mathbf{x}} \cdot [\mathbf{v} p_t] = \sum_{i=1}^d \frac{\partial}{\partial x_i} [v_i p_t]$ is the divergence operator and we take advantage of the divergence theorem and used integration by parts to get the second equality. By the properties of Fourier transform, Eq. (23) implies that $p_t(\mathbf{x})$ satisfies the transport equation

$$\partial_t p_t(\mathbf{x}) + \nabla_{\mathbf{x}} \cdot (\mathbf{v}(\mathbf{x}, t) p_t(\mathbf{x})) = 0. \quad (24)$$

Solving this equation by the method of characteristic leads to probability flow ODE (2).

A.2. Proof of the SDE (4)

We show that the SDE (4) has marginal density $p_t(\mathbf{x})$ with any choice of $w_t \geq 0$. To this end, recall that solution to the SDE

$$d\mathbf{X}_t = [\mathbf{v}(\mathbf{X}_t, t) + \frac{1}{2} w_t \mathbf{s}(\mathbf{X}_t, t)] dt + \sqrt{w_t} d\bar{\mathbf{W}}_t$$

has a PDF that satisfies the Fokker-Planck equation

$$\partial_t p_t(\mathbf{x}) = -\nabla_{\mathbf{x}} \cdot \left([\mathbf{v}(\mathbf{x}, t) + \frac{1}{2} w_t \mathbf{s}(\mathbf{x}, t)] p_t(\mathbf{x}) \right) + \frac{1}{2} w_t \Delta_{\mathbf{x}} p_t(\mathbf{x}) \quad (25)$$

where $\Delta_{\mathbf{x}}$ is the Laplace operator defined as $\Delta_{\mathbf{x}} = \nabla_{\mathbf{x}} \cdot \nabla_{\mathbf{x}} = \sum_{i=0}^d \frac{\partial^2}{\partial x_i^2}$. Reorganizing the equation and using the definition of the score $\mathbf{s}(\mathbf{x}, t) = \nabla_{\mathbf{x}} \log p_t(\mathbf{x}) = p_t^{-1}(\mathbf{x}) \nabla_{\mathbf{x}} p_t(\mathbf{x})$, we have

$$\partial_t p_t(\mathbf{x}) = \underbrace{-\nabla_{\mathbf{x}} \cdot [\mathbf{v}(\mathbf{x}, t) p_t(\mathbf{x})]}_{= \partial_t p_t(\mathbf{x}) \text{ by Eq. (24)}} - \frac{1}{2} w_t \nabla_{\mathbf{x}} \cdot \underbrace{[\nabla_{\mathbf{x}} \log p_t(\mathbf{x}) p_t(\mathbf{x})]}_{= \nabla_{\mathbf{x}} p_t(\mathbf{x})} + \frac{1}{2} w_t \Delta_{\mathbf{x}} p_t(\mathbf{x}) \quad (26)$$

$$\implies 0 = -\frac{1}{2} w_t \nabla_{\mathbf{x}} \cdot \nabla_{\mathbf{x}} p_t(\mathbf{x}) + \frac{1}{2} w_t \Delta_{\mathbf{x}} p_t(\mathbf{x}) \quad (27)$$

By definition of Laplace operator, the last equation holds for any $w_t \geq 0$. When $w_t = 0$, the Fokker-Planck equation reduces to a continuity equation, and the SDE reduces to an ODE, so the connection trivially holds.

A.3. Proof of the expression for the score in Eq. (5)

We show that $\mathbf{s}(\mathbf{x}, t) = -\sigma_t^{-1} \mathbb{E}[\boldsymbol{\varepsilon} | \mathbf{x}_t = \mathbf{x}]$. Letting $\hat{f}(\mathbf{k}, t) = \mathbb{E}[\boldsymbol{\varepsilon} e^{i\sigma_t \mathbf{k} \cdot \boldsymbol{\varepsilon}}]$, we have

$$\hat{f}(\mathbf{k}, t) = -\frac{i}{\sigma_t} \nabla_{\mathbf{k}} \mathbb{E}[e^{i\sigma_t \mathbf{k} \cdot \boldsymbol{\varepsilon}}] \quad (28)$$

Since $\boldsymbol{\varepsilon} \sim \mathcal{N}(0, \mathbf{I})$, we can compute the expectation explicitly to obtain

$$\hat{f}(\mathbf{k}, t) = -\frac{i}{\sigma_t} (\nabla_{\mathbf{k}} e^{-\frac{1}{2}\sigma_t^2 |\mathbf{k}|^2}) \quad (29)$$

$$= i\sigma_t \mathbf{k} e^{-\frac{1}{2}\sigma_t^2 |\mathbf{k}|^2} \quad (30)$$

Since \mathbf{x}_* and $\boldsymbol{\varepsilon}$ are independent random variable, we have

$$\mathbb{E}[\boldsymbol{\varepsilon} e^{i\mathbf{k} \cdot \mathbf{x}_t}] = \hat{f}(\mathbf{k}, t) \mathbb{E}[e^{i\alpha_t \mathbf{k} \cdot \mathbf{x}_*}] = i\sigma_t \mathbf{k} \underbrace{e^{-\frac{1}{2}\sigma_t^2 |\mathbf{k}|^2} \mathbb{E}[e^{i\alpha_t \mathbf{k} \cdot \mathbf{x}_*}]}_{\text{combine this}} = i\sigma_t \mathbf{k} \hat{p}_t(\mathbf{k}) \quad (31)$$

where $\hat{p}_t(\mathbf{k})$ is the characteristic function of $\mathbf{x}_t = \alpha_t \mathbf{x}_* + \sigma_t \boldsymbol{\varepsilon}$ defined in Eq. (16). The left hand-side of this equation can also be written as:

$$\mathbb{E}[\boldsymbol{\varepsilon} e^{i\mathbf{k} \cdot \mathbf{x}_t}] = \int_{\mathbb{R}^d} \mathbb{E}[\boldsymbol{\varepsilon} e^{i\mathbf{k} \cdot \mathbf{x}_t} | \mathbf{x}_t = \mathbf{x}] p_t(\mathbf{x}) d\mathbf{x} \quad (32)$$

$$= \int_{\mathbb{R}^d} \mathbb{E}[\boldsymbol{\varepsilon} | \mathbf{x}_t = \mathbf{x}] e^{i\mathbf{k} \cdot \mathbf{x}} p_t(\mathbf{x}) d\mathbf{x}, \quad (33)$$

whereas the right hand-side is

$$i\sigma_t \mathbf{k} \hat{p}_t(\mathbf{k}) = i\sigma_t \mathbf{k} \int_{\mathbb{R}^d} e^{i\mathbf{k} \cdot \mathbf{x}} p_t(\mathbf{x}) d\mathbf{x} \quad (34)$$

$$= \sigma_t \int_{\mathbb{R}^d} \nabla_{\mathbf{x}} [e^{i\mathbf{k} \cdot \mathbf{x}}] p_t(\mathbf{x}) d\mathbf{x} \quad (35)$$

$$= -\sigma_t \int_{\mathbb{R}^d} e^{i\mathbf{k} \cdot \mathbf{x}} \nabla_{\mathbf{x}} p_t(\mathbf{x}) d\mathbf{x} \quad (36)$$

$$= -\sigma_t \int_{\mathbb{R}^d} e^{i\mathbf{k} \cdot \mathbf{x}} \mathbf{s}(\mathbf{x}, t) p_t(\mathbf{x}) d\mathbf{x} \quad (37)$$

where we again used divergence theorem and integration by parts to get the third equality, and again the definition of the score to get the last. Comparing Eq. (33) and Eq. (37) we deduce that, when $\sigma_t \neq 0$,

$$\mathbf{s}(\mathbf{x}, t) = \nabla_{\mathbf{x}} \log p_t(\mathbf{x}) = -\sigma_t^{-1} \mathbb{E}[\boldsymbol{\varepsilon} | \mathbf{x}_t = \mathbf{x}] \quad (38)$$

Further, setting w_t to σ_t in Eq. (4) gives

$$\frac{1}{2} w_t \mathbf{s}(\mathbf{x}_t, t) = -\frac{1}{2} \mathbb{E}[\boldsymbol{\varepsilon} | \mathbf{x}_t = \mathbf{x}] \quad (39)$$

for all $t \in [0, 1]$. This bypass the constraint of $\sigma_t \neq 0$ and effectively eliminate the singularity at $t = 0$.

A.4. Proof of Eq. (9)

We note that there exists a straightforward connection between $\mathbf{v}(\mathbf{x}, t)$ and $\mathbf{s}(\mathbf{x}, t)$. From Eq. (1), we have

$$\mathbf{v}(\mathbf{x}, t) = \dot{\alpha}_t \mathbb{E}[\mathbf{x}_* | \mathbf{x}_t = \mathbf{x}] + \dot{\sigma}_t \mathbb{E}[\boldsymbol{\varepsilon} | \mathbf{x}_t = \mathbf{x}] \quad (40)$$

$$= \dot{\alpha}_t \mathbb{E}\left[\frac{\mathbf{x}_t - \sigma_t \boldsymbol{\varepsilon}}{\alpha_t} | \mathbf{x}_t = \mathbf{x}\right] + \dot{\sigma}_t \mathbb{E}[\boldsymbol{\varepsilon} | \mathbf{x}_t = \mathbf{x}] \quad (41)$$

$$= \frac{\dot{\alpha}_t}{\alpha_t} \mathbf{x} + \left(\dot{\sigma}_t - \frac{\dot{\alpha}_t \sigma_t}{\alpha_t}\right) \mathbb{E}[\boldsymbol{\varepsilon} | \mathbf{x}_t = \mathbf{x}] \quad (42)$$

$$= \frac{\dot{\alpha}_t}{\alpha_t} \mathbf{x} + \left(\dot{\sigma}_t - \frac{\dot{\alpha}_t \sigma_t}{\alpha_t}\right) (-\sigma_t \mathbf{s}(\mathbf{x}, t)) \quad (43)$$

$$= \frac{\dot{\alpha}_t}{\alpha_t} \mathbf{x} - \lambda_t \sigma_t \mathbf{s}(\mathbf{x}, t) \quad (44)$$

where we defined

$$\lambda_t = \dot{\sigma}_t - \frac{\dot{\alpha}_t \sigma_t}{\alpha_t} \quad (45)$$

Given Eq. (44) is linear in terms of \mathbf{s} , reverting it will lead to Eq. (9).

Note that we can also plug Eq. (44) into the loss \mathcal{L}_v in Eq. (7) to deduce that

$$\mathcal{L}_v(\theta) = \int_0^T \mathbb{E}\left[\left\|\frac{\dot{\alpha}_t}{\alpha_t} \mathbf{x} + \lambda_t (-\sigma_t \mathbf{s}_\theta(\mathbf{x}_t, t)) - \dot{\alpha}_t \mathbf{x}_* - \dot{\sigma}_t \boldsymbol{\varepsilon}\right\|^2\right] dt \quad (46)$$

Expand to $\mathbf{x}_t = \alpha_t \mathbf{x}_* + \sigma_t \boldsymbol{\varepsilon}$

$$= \int_0^T \mathbb{E}\left[\left\|\dot{\alpha}_t \mathbf{x}_* + \frac{\dot{\alpha}_t \sigma_t}{\alpha_t} \boldsymbol{\varepsilon} + \lambda_t (-\sigma_t \mathbf{s}_\theta(\mathbf{x}_t, t)) - \dot{\alpha}_t \mathbf{x}_* - \dot{\sigma}_t \boldsymbol{\varepsilon}\right\|^2\right] dt \quad (47)$$

$$= \int_0^T \mathbb{E}\left[\left\|\lambda_t (-\sigma_t \mathbf{s}_\theta(\mathbf{x}_t, t)) - \lambda_t \boldsymbol{\varepsilon}\right\|^2\right] dt \quad (48)$$

$$= \int_0^T \lambda_t^2 \mathbb{E}\left[\left\|\sigma_t \mathbf{s}_\theta(\mathbf{x}_t, t) + \boldsymbol{\varepsilon}\right\|^2\right] dt \quad (49)$$

$$\equiv \mathcal{L}_{s_\lambda}(\theta) \quad (50)$$

which defines the weighted score objective $\mathcal{L}_{s_\lambda}(\theta)$. This observation is consistent with the claim made in Kingma and Gao [35] that the score objective with different monotonic weighting functions coincides with losses for different model parameterizations. In Appendix B we show that λ_t corresponds to the square of the maximum likelihood weighting proposed in Song et al. [61] and Vahdat et al. [65].

B. Connection with Score-based Diffusion

As shown in Song et al. [62], the reverse-time SDE from Eq. (10) is

$$d\mathbf{X}_t = \left[-\frac{1}{2}\beta_t \mathbf{X}_t - \beta_t \mathbf{s}(\mathbf{X}_t, t)\right] dt + \sqrt{\beta_t} d\bar{\mathbf{W}}_t \quad (51)$$

Let us show this SDE is Eq. (4) for the specific choice $w_t = \beta_t$. To this end, notice that the solution \mathbf{X}_t to Eq. (51) for the initial condition $\mathbf{X}_{t=0} = \mathbf{x}_*$ with \mathbf{x}_* fixed is Gaussian distributed with mean and variance given respectively by

$$\mathbb{E}[\mathbf{X}_t] = e^{-\frac{1}{2} \int_0^t \beta_s ds} \mathbf{x}_* \equiv \alpha_t \mathbf{x}_* \quad (52)$$

$$\text{var}[\mathbf{X}_t] = 1 - e^{-\int_0^t \beta_s ds} \equiv \sigma_t^2 \quad (53)$$

Using Eq. (44), the velocity of the score-based diffusion model can therefore be expressed as

$$\mathbf{v}(\mathbf{x}, t) = -\frac{1}{2}\beta_t \mathbf{x} + \left(-\frac{1}{2}\beta_t (1 - e^{-\int_0^t \beta_s ds}) - \frac{1}{2}\beta_t e^{-\int_0^t \beta_s ds}\right) \mathbf{s}(\mathbf{x}, t) \quad (54)$$

$$= -\frac{1}{2}\beta_t \mathbf{x} - \frac{1}{2}\beta_t \mathbf{s}(\mathbf{x}, t) \quad (55)$$

we see that $2\lambda_t \sigma_t$ is precisely β_t , making λ_t correspond to the square of maximum likelihood weighting proposed in Song et al. [62]. Further, if we plug Eq. (55) into Eq. (4) with $w_t = \beta_t$, we arrive at Eq. (51).

A useful observation for choosing velocity versus noise model. We see that in the velocity model, all of the path-dependent terms (α_t, σ_t) are inside the squared loss, and in the score model, the terms are pulled out (apart from the necessary σ_t in score matching loss) and get squared due to coming out of the norm. So which is more stable depends on the interpolant. In the paper we see that for SBDM-VP, due to the blowing up behavior of $\dot{\sigma}_t$ near $t = 0$, both \mathcal{L}_v and \mathcal{L}_{s_λ} are unstable.

Yet, shown in Tab. 5, we observed better performance with \mathcal{L}_{s_λ} for SBDM-VP, as the blowing up λ_t near $t = 0$ will compensate for the diminishing gradient inside the squared norm, where \mathcal{L}_v would simply experience gradient explosion resulted from $\dot{\sigma}_t$. The behavior is different for the Linear and GVP interpolant, where the source of instability is α_t^{-1} near $t = 1$. We note \mathcal{L}_v is stable since α_t^{-1} gets cancelled out inside the squared norm, while in \mathcal{L}_{s_λ} it remains in λ_t outside the norm.

C. Sampling with Guidance

Let $p_t(\mathbf{x}|\mathbf{y})$ be the density of $\mathbf{x}_t = \alpha_t \mathbf{x}_* + \sigma_t \varepsilon$ conditioned on some extra variable \mathbf{y} . By argument similar to the one given in Appendix A.1, it is easy to see that $p_t(\mathbf{x}|\mathbf{y})$ satisfies the transport equation (compare Eq. (24))

$$\partial_t p_t(\mathbf{x}|\mathbf{y}) + \nabla_{\mathbf{x}} \cdot (\mathbf{v}(\mathbf{x}, t|\mathbf{y}) p_t(\mathbf{x}, |\mathbf{y})) = 0, \quad (56)$$

where (compare Eq. (3))

$$\mathbf{v}(\mathbf{x}, t|\mathbf{y}) = \mathbb{E}[\dot{\mathbf{x}}_t | \mathbf{x}_t = \mathbf{x}, \mathbf{y}] = \dot{\alpha}_t \mathbb{E}[\mathbf{x}_* | \mathbf{x}_t = \mathbf{x}, \mathbf{y}] + \dot{\sigma}_t \mathbb{E}[\varepsilon | \mathbf{x}_t = \mathbf{x}, \mathbf{y}] \quad (57)$$

Proceeding as in Appendix A.3 and Appendix A.4, it is also easy to see that the score $\mathbf{s}(\mathbf{x}, t|\mathbf{y}) = \nabla_{\mathbf{x}} \log p_t(\mathbf{x}|\mathbf{y})$ is given by (compare Eq. (5))

$$\mathbf{s}(\mathbf{x}, t|\mathbf{y}) = -\sigma_t^{-1} \mathbb{E}[\varepsilon | \mathbf{x}_t = \mathbf{x}, \mathbf{y}] \quad (58)$$

and that $\mathbf{v}(\mathbf{x}, t|\mathbf{y})$ and $\mathbf{s}(\mathbf{x}, t|\mathbf{y})$ are related via (compare Eq. (44))

$$\mathbf{v}(\mathbf{x}, t|\mathbf{y}) = \frac{\dot{\alpha}_t}{\alpha_t} \mathbf{x} - \lambda_t \sigma_t \mathbf{s}(\mathbf{x}, t|\mathbf{y}) \quad (59)$$

Consider now

$$\mathbf{s}^\zeta(\mathbf{x}, t|\mathbf{y}) \equiv (1 - \zeta) \mathbf{s}(\mathbf{x}, t) + \zeta \mathbf{s}(\mathbf{x}, t|\mathbf{y}) \quad (60)$$

$$= \nabla \log p_t(\mathbf{x}) - \zeta \nabla \log p_t(\mathbf{x}) + \zeta \nabla \log p_t(\mathbf{x}|\mathbf{y}) \quad (61)$$

$$= \nabla \log p_t(\mathbf{x}) - \zeta \nabla \log p_t(\mathbf{x}) + \left(\zeta \nabla \log p_t(\mathbf{y}|\mathbf{x}) + \zeta \nabla \log p_t(\mathbf{x}) \right) \quad (62)$$

$$= \nabla \log p_t(\mathbf{x}) + \zeta \nabla \log p_t(\mathbf{y}|\mathbf{x}) \quad (63)$$

$$= \nabla \log [p_t(\mathbf{x}) p_t^\zeta(\mathbf{y}|\mathbf{x})] \quad (64)$$

where we have used the fact $\nabla_{\mathbf{x}} \log p_t(\mathbf{x}|\mathbf{y}) = \nabla_{\mathbf{x}} \log p_t(\mathbf{y}|\mathbf{x}) + \nabla_{\mathbf{x}} \log p_t(\mathbf{x})$ that follows from $p_t(\mathbf{x}|\mathbf{y}) p(\mathbf{y}) = p_t(\mathbf{y}|\mathbf{x}) p_t(\mathbf{x})$, and ζ to be some constant greater than 1. Eq. (64) shows that using the score mixture $\mathbf{s}^\zeta(\mathbf{x}, t|\mathbf{y}) = (1 - \zeta) \mathbf{s}(\mathbf{x}, t) + \zeta \mathbf{s}(\mathbf{x}, t|\mathbf{y})$, and the velocity mixture associated with it, namely,

$$\mathbf{v}^\zeta(\mathbf{x}, t|\mathbf{y}) = (1 - \zeta) \mathbf{v}(\mathbf{x}, t) + \zeta \mathbf{v}(\mathbf{x}, t|\mathbf{y}) \quad (65)$$

$$= \frac{\dot{\alpha}_t}{\alpha_t} \mathbf{x} - \lambda_t \sigma_t [(1 - \zeta) \mathbf{s}(\mathbf{x}, t) + \zeta \mathbf{s}(\mathbf{x}, t|\mathbf{y})] \quad (66)$$

$$= \frac{\dot{\alpha}_t}{\alpha_t} \mathbf{x} - \lambda_t \sigma_t \mathbf{s}^\zeta(\mathbf{x}, t|\mathbf{y}), \quad (67)$$

allows one to to construct generative models that sample the tempered distribution $p_t(\mathbf{x}_t) p_t^\zeta(\mathbf{y}|\mathbf{x}_t)$ following classifier guidance [19]. Note that $p_t(\mathbf{x}) p_t^\zeta(\mathbf{y}|\mathbf{x}) \propto p_t^\zeta(\mathbf{x}|\mathbf{y}) p_t^{1-\zeta}(\mathbf{x})$, so we can also perform classifier free guidance sampling [24]. Empirically, we observe significant performance boost by applying classifier free guidance, as showed in Tab. 1 and Tab. 9.

| Model | Training Steps(K) | FID↓ | sFID↓ | IS↑ | Precision↑ | Recall↑ |
|--------|-------------------|---------------|-------------|-----------------|-------------|-------------|
| SiT-S | 400 | 58.97 / 57.64 | 8.95 / 9.05 | 23.34 / 24.78 | 0.40 / 0.41 | 0.59 / 0.60 |
| SiT-B | 400 | 34.84 / 33.45 | 6.59 / 6.46 | 41.53 / 43.71 | 0.52 / 0.53 | 0.64 / 0.63 |
| SiT-L | 400 | 20.01 / 18.79 | 5.31 / 5.29 | 67.76 / 72.02 | 0.62 / 0.64 | 0.64 / 0.64 |
| SiT-XL | 400 | 18.04 / 17.19 | 5.17 / 5.07 | 73.90 / 76.52 | 0.63 / 0.65 | 0.64 / 0.63 |
| SiT-XL | 7000 | 9.35 / 8.61 | 6.38 / 6.32 | 126.06 / 131.65 | 0.67 / 0.68 | 0.68 / 0.67 |

Table 1. **FID-50K scores produced by ODE and SDE.** We demonstrate the comparison between ODE and SDE across all of our model sizes. All statistics are produced without classifier free guidance. Each cell in the table is showing [ODE results] / [SDE results]. We note the better performances of SDE observed in all model sizes are in line with the bounds given in [3], and that ODE has its advantage in lower NFE region, as shown in Fig. 5

D. Sampling with ODE and SDE

In the main body of the paper, we used a Heun integrator for solving the ODE in Eq. (2) and an Euler-Maruyama integrator for solving the SDE in Eq. (4). We summarize all results in Tab. 1, and present the implementations below.

Algorithm 1 Deterministic Heun Sampler

```

procedure HEUNSAMPLER( $\mathbf{v}_\theta(\mathbf{x}, t, \mathbf{y}), t_{i \in \{0, \dots, N\}}, \alpha_t, \sigma_t$ )
  sample  $\mathbf{x}_0 \sim \mathcal{N}(0, \mathbf{I})$  ▷ Generate initial sample
   $\Delta t \leftarrow t_1 - t_0$  ▷ Determine fixed step size
  for  $i \in \{0, \dots, N - 1\}$  do
     $\mathbf{d}_i \leftarrow \mathbf{v}_\theta(\mathbf{x}_i, t_i, \mathbf{y})$ 
     $\bar{\mathbf{x}}_{i+1} \leftarrow \mathbf{x}_i + \Delta t \mathbf{d}_i$  ▷ Euler Step at  $t_i$ 
     $\mathbf{d}_{i+1} \leftarrow \mathbf{v}_\theta(\bar{\mathbf{x}}_{i+1}, t_{i+1}, \mathbf{y})$ 
     $\mathbf{x}_{i+1} \leftarrow \mathbf{x}_i + \frac{\Delta t}{2} [\mathbf{d}_i + \mathbf{d}_{i+1}]$  ▷ Explicit trapezoidal rule at  $t_{i+1}$ 
  end for
  return  $\mathbf{x}_N$ 
end procedure

```

Algorithm 2 Stochastic Euler-Maruyama Sampler

```

procedure EULERSAMPLER( $\mathbf{v}_\theta(\mathbf{x}, t, \mathbf{y}), w_t, t_{i \in \{0, \dots, N\}}, T, \alpha_t, \sigma_t$ )
  sample  $\mathbf{x}_0 \sim \mathcal{N}(0, \mathbf{I})$  ▷ Generate initial sample
   $\mathbf{s}_\theta \leftarrow$  convert from  $\mathbf{v}_\theta$  following Appendix A.4 ▷ Obtain  $\nabla_{\mathbf{x}} \log p_t(\mathbf{x})$  in Eq. (4)
   $\Delta t \leftarrow t_1 - t_0$  ▷ Determine fixed step size
  for  $i \in \{0, \dots, N - 1\}$  do
    sample  $\boldsymbol{\varepsilon}_i \sim \mathcal{N}(0, \mathbf{I})$ 
     $d\boldsymbol{\varepsilon}_i \leftarrow \boldsymbol{\varepsilon}_i * \sqrt{\Delta t}$ 
     $\mathbf{d}_i \leftarrow \mathbf{v}_\theta(\mathbf{x}_i, t_i, \mathbf{y}) + \frac{1}{2} w_{t_i} \mathbf{s}_\theta(\mathbf{x}_i, t_i, \mathbf{y})$  ▷ Evaluate drift term at  $t_i$ 
     $\bar{\mathbf{x}}_{i+1} \leftarrow \mathbf{x}_i + \Delta t \mathbf{d}_i$ 
     $\mathbf{x}_{i+1} \leftarrow \bar{\mathbf{x}}_{i+1} + \sqrt{w_{t_i}} d\boldsymbol{\varepsilon}_i$  ▷ Evaluate diffusion term at  $t_i$ 
  end for
   $h \leftarrow T - t_N$  ▷ Last step size;  $T$  denotes the time where  $\mathbf{x}_T = \mathbf{x}_*$ 
   $\mathbf{d} \leftarrow \mathbf{v}_\theta(\mathbf{x}_N, t_N, \mathbf{y}) + \frac{1}{2} w_{t_N} \mathbf{s}_\theta(\mathbf{x}_N, t_N, \mathbf{y})$ 
   $\mathbf{x} \leftarrow \mathbf{x}_N + h * \mathbf{d}$  ▷ Last step; output noiseless sample without diffusion
  return  $\mathbf{x}$ 
end procedure

```

It is feasible to use either a velocity model \mathbf{v}_θ or a score model \mathbf{s}_θ in applying the above two samplers. If learning the score

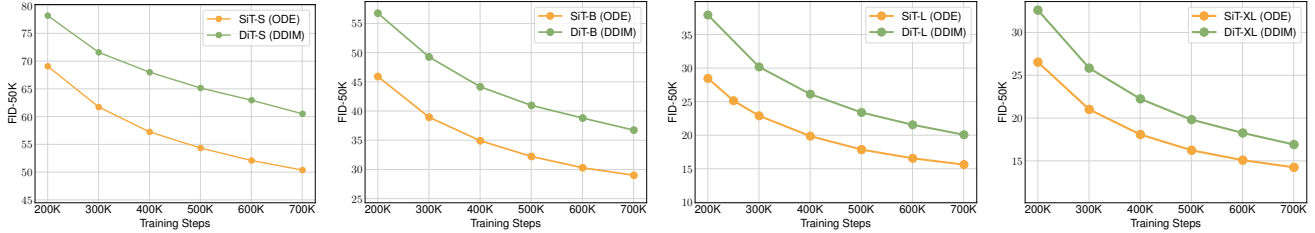


Figure 1. **SiT observes improvement in FID across all model sizes.** We show FID-50K over training iterations for both DiT and SiT models. Across all model sizes, SiT converges faster. We acknowledge this is *not directly an apples-to-apples comparison*. This is because DDIM is essentially a discrete form of the first-order Euler’s method, whereas in sampling SiT, we employ the second-order Heun’s method. Nevertheless, both the SiT and DiT results are produced by a deterministic sampler with a 250 NFE.

for the deterministic Heun sampler, we could always convert the learned \mathbf{s}_θ to \mathbf{v}_θ following Appendix A.4. However, as there exists potential numerical instability (depending on interpolants) in $\dot{\sigma}_t$, α_t^{-1} and λ_t , it’s recommended to learn \mathbf{v}_θ in sampling with deterministic sampler instead of \mathbf{s}_θ . For the stochastic sampler, it’s required to have both \mathbf{v}_θ and \mathbf{s}_θ in integration, so we always need to convert from one (either learning velocity or score) to obtain the other. Under this scenario, the numerical issue from Appendix A.4 can only be avoided by clipping the time interval near $t = 0$. Empirically we found clipping the interval by $h = 0.04$ and doing a long last step from $t = 0.04$ to 0 can greatly benefit the performance. A detailed summary of sampler configuration is provided in Appendix E.

Additionally, we could replace \mathbf{v}_θ and \mathbf{s}_θ by \mathbf{v}_θ^ζ and \mathbf{s}_θ^ζ presented in Appendix C as inputs of the two samplers and enjoy the performance improvements coming along with guidance. As guidance requires evaluating both conditional and unconditional model output in a single step, it will impose twice the computational cost when sampling.

Comparison between DDPM and Euler-Maruyama We primarily investigate and report the performance comparison between DDPM and Euler-Maruyama samplers. We set our Euler sampler’s number of steps to be 250 to match that of DDPM during evaluation. This comparison is made direct and fair, as the DDPM method is equivalent to a discretized Euler’s method.

Comparison between DDIM and Heun We also investigate the performance difference produced by deterministic samplers between DiT and our models. In Fig. 1, we show the FID-50K results for both DiT models sampled with DDIM and SiT models sampled with Heun. We note that this is not directly an apples-to-apples comparison, as DDIM can be viewed as a discretized version of the first order Euler’s method, while we use the second order Heun’s method in sampling SiT models, due to the large discretization error with Euler’s method in continuous time. Nevertheless, we control the NFEs for both DDIM (250 sampling steps) and Heun (250 NFE).

Higher order solvers The performances of an adaptive deterministic `dopri5` solver and a second order stochastic Heun Sampler [32] are also tested. For `dopri5`, we set `atol` and `rtol` to $1e-6$ and $1e-3$, respectively; for Heun, we again maintain the NFE to be 250 to match that of DDPM. In both solvers we do not observe performance increment; under the CFG scale of $\zeta = 1.5$, `dopri5` and stochastic Heun gives FID-50K of 2.15 and 2.07, respectively.

We also note that our models are compatible with other samplers [36, 44] specifically tuned to diffusion models as well as sampling distillation [54, 63]. We do not include the evaluations of those methods in our work for the sake of apples-to-apples comparison with the DDPM model, and we leave the investigation of potential performance improvements to future work.

E. Additional Implementation Details

We implemented our models in JAX following the DiT PyTorch codebase by Peebles and Xie [48]⁴, and referred to Albergo et al. [3]⁵, Song et al. [62]⁶, and Dockhorn et al. [20]⁷ for our implementation of the Euler-Maruyama sampler. For the Heun sampler, we directly used the one from `diffraX` [33]⁸, a JAX-based numerical differential equation solver library.

⁴<https://github.com/facebookresearch/DiT>

⁵<https://github.com/malbergo/stochastic-interpolants>

⁶https://github.com/yang-song/score_sde

⁷<https://github.com/nv-tlabs/CLD-SGM>

⁸<https://github.com/patrick-kidger/diffraX>

Training configurations We trained all of our models following identical structure and hyperparameters retained from DiT [48]. We used AdamW [34, 43] as optimizer for all models. We use a constant learning rate of 1×10^{-4} and a batch size of 256. We used random horizontal flip with probability of 0.5 in data augmentation. *We did not tune the learning rates, decay/warm up schedules, AdamW parameters, nor use any extra data augmentation or gradient clipping during training.* Our largest model, SiT-XL, trains at approximately 6.8 iters/sec on a TPU v4-64 pod following the above configurations. This speed is slightly faster compared to DiT-XL, which trains at 6.4 iters/sec under identical settings. We also gather the training speed of other model sizes and summarize them below.

| | S | B | L | XL |
|-----|------|------|-----|-----|
| DiT | 20.0 | 19.8 | 9.3 | 6.4 |
| SiT | 19.7 | 20.8 | 9.3 | 6.8 |

Table 2. **Training speed (iters/sec) across all model sizes.** All training speeds are measured on a TPU v4-64 pod. *We note that the training speed is largely influenced by the hardware state.*

Sampling configurations We maintain an exponential moving average (EMA) of all models weights over training with a decay of 0.9999. All results are sampled from the EMA checkpoints, which is empirically observed to yield better performance. We summarize the start and end points of our deterministic and stochastic samplers with different interpolants below, where each t_0 and t_N are carefully tuned to optimize performance and avoid numerical instability during integration.

| Interpolant | Model | Objective | Heun | | Euler-Maruyama | |
|-------------|----------|---------------------------|------------|--------|----------------|--------|
| | | | t_0 | t_N | t_0 | t_N |
| SBDM-VP | velocity | \mathcal{L}_v | 1 | $1e-5$ | 1 | $4e-2$ |
| | score | \mathcal{L}_{s_λ} | 1 | $1e-5$ | 1 | $4e-2$ |
| GVP | velocity | \mathcal{L}_v | 1 | 0 | 1 | $4e-2$ |
| | score | \mathcal{L}_s | $1 - 1e-5$ | 0 | $1 - 1e-3$ | $4e-2$ |
| Linear | velocity | \mathcal{L}_v | 1 | 0 | 1 | $4e-2$ |
| | score | \mathcal{L}_s | $1 - 1e-5$ | 0 | $1 - 1e-3$ | $4e-2$ |

Table 3. Sampler configurations

FID calculation We calculate FID scores between generated images (10K or 50K) and all available real images in ImageNet training dataset. We observe small performance variations between TPU-based FID evaluation and GPU-based FID evaluation (ADM’s TensorFlow evaluation suite [19]⁹). To ensure consistency with the baseline DiT, we sample all of our models on GPU and obtain FID scores using the ADM evaluation suite.

⁹<https://github.com/openai/guided-diffusion/tree/main/evaluations>

F. Additional Visual results



Figure 2. **Uncurated** 512×512 SiT-XL samples.
Classifier-free guidance scale = 4.0
Class label = "volcano"(980)



Figure 3. **Uncurated** 512×512 SiT-XL samples.
Classifier-free guidance scale = 4.0
Class label = "arctic fox"(279)



Figure 4. **Uncurated** 512×512 SiT-XL samples.
 Classifier-free guidance scale = 4.0
 Class label = "loggerhead turtle"(33)



Figure 5. **Uncurated** 512×512 SiT-XL samples.
 Classifier-free guidance scale = 4.0
 Class label = "balloon"(417)

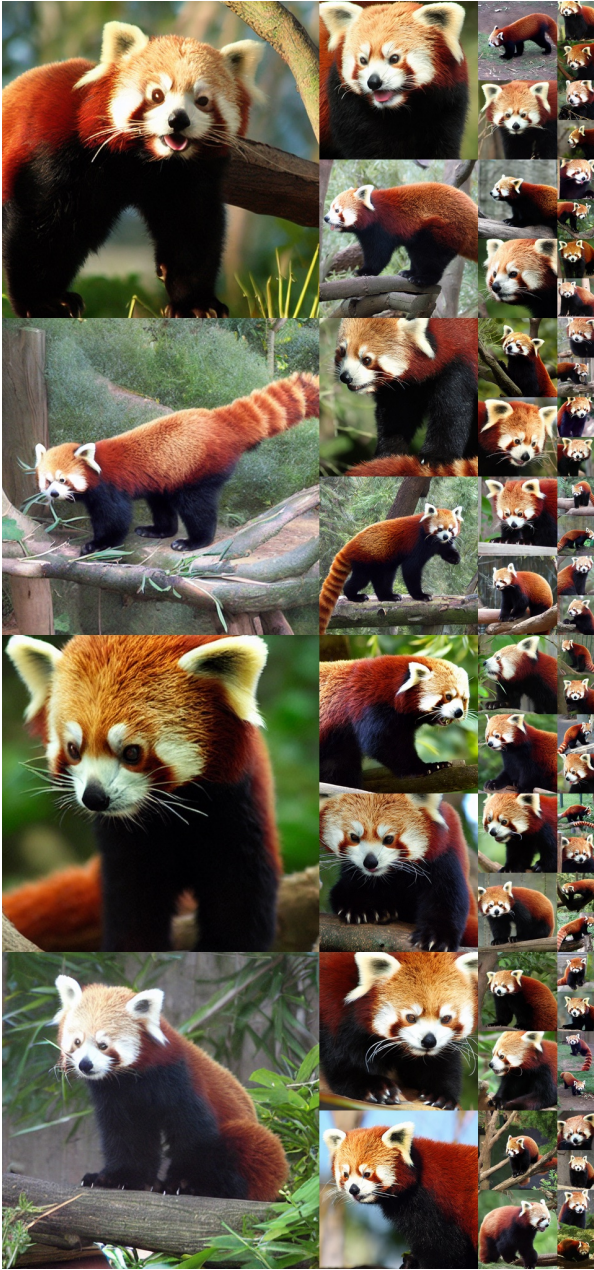


Figure 6. **Uncrated** 512×512 SiT-XL samples.
 Classifier-free guidance scale = 4.0
 Class label = "red panda"(387)



Figure 7. **Uncrated** 512×512 SiT-XL samples.
 Classifier-free guidance scale = 4.0
 Class label = "geyser"(974)



Figure 8. **Uncurated** 256×256 SiT-XL samples.
 Classifier-free guidance scale = 4.0
 Class label = "macaw"(88)



Figure 9. **Uncurated** 256×256 SiT-XL samples.
 Classifier-free guidance scale = 4.0
 Class label = "golden retriever"(207)



Figure 10. **Uncurated** 256×256 SiT-XL samples.
 Classifier-free guidance scale = 4.0
 Class label = "ice cream"(928)

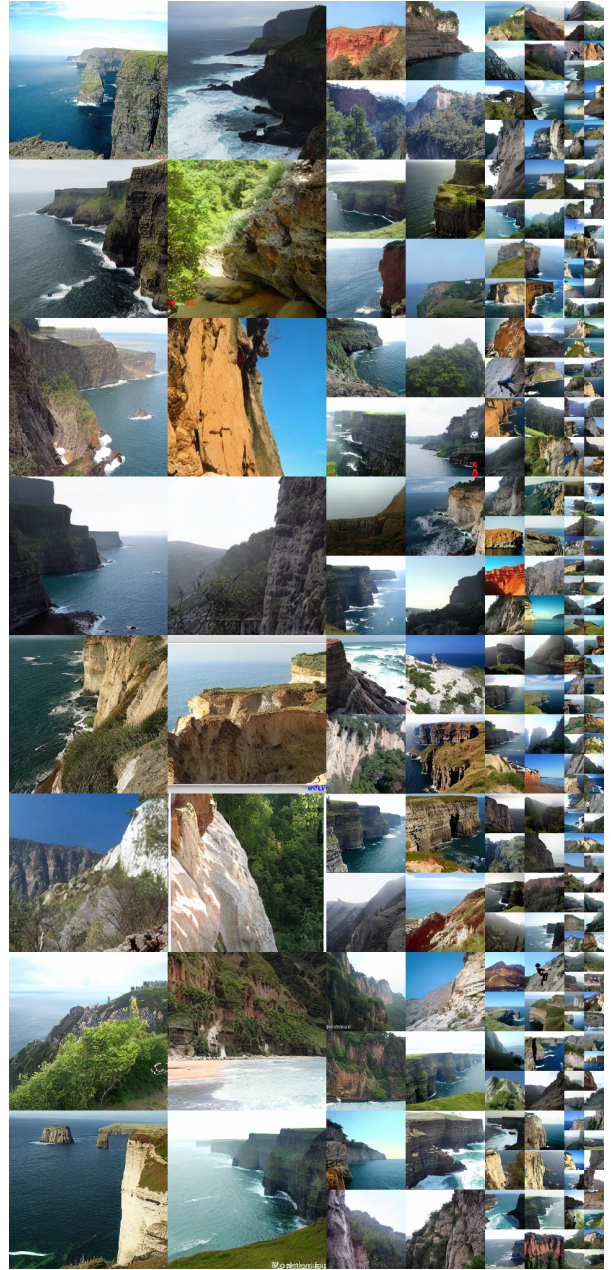


Figure 11. **Uncurated** 256×256 SiT-XL samples.
 Classifier-free guidance scale = 4.0
 Class label = "cliff"(972)

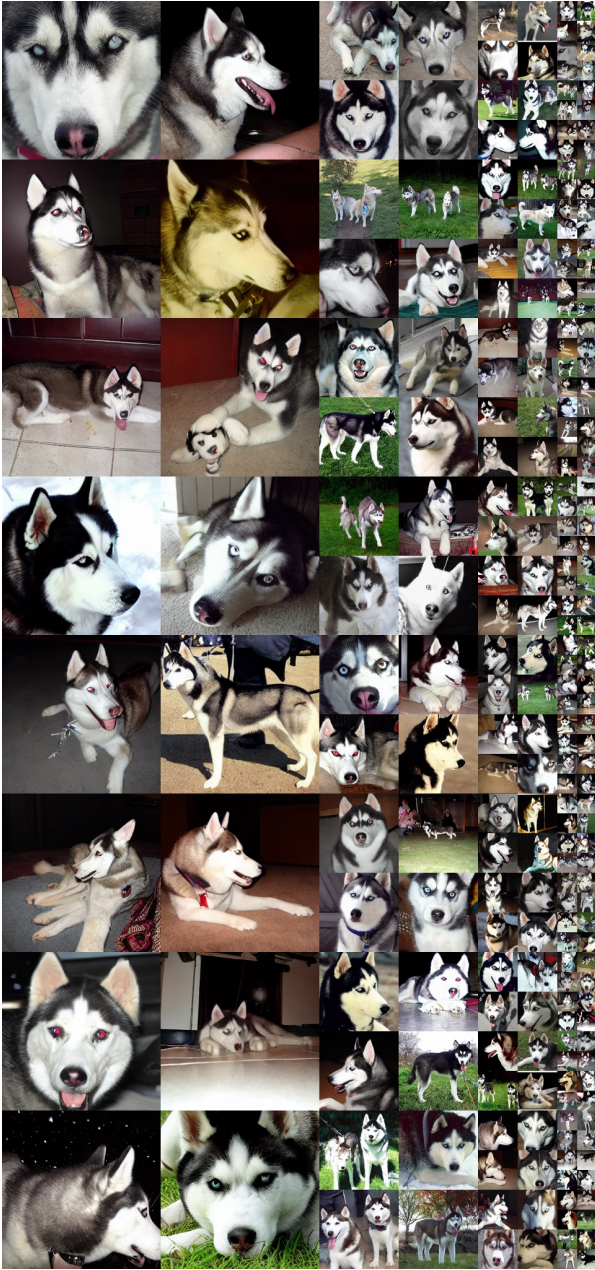


Figure 12. **Uncurated** 256×256 SiT-XL samples.
 Classifier-free guidance scale = 4.0
 Class label = "husky"(250)



Figure 13. **Uncurated** 256×256 SiT-XL samples.
 Classifier-free guidance scale = 4.0
 Class label = "valley"(979)